RSC Advances

PAPER

View Article Online
View Journal | View Issue

Cite this: *RSC Adv.*, 2023, **13**, 25081

Effect of bismuth doping on the crystal structure and photocatalytic activity of titanium oxide

Dina A. Tolan,[ab] Ayman K. El-Sawaf,*[ab] Islam G. Alhindawy,[c] Mohamed H. Ismael,[c] Amal A. Nassar,[a] Ahmed M. El-Nahas,[b] Mai Maize,[b] Emad A. Elshehy[c] and Mohamed E. El-Khouly[d]

The doping of TiO_2 with metals and non-metals is considered one of the most significant approaches to improve its photocatalytic efficiency. In this study, the photodegradation of methyl orange (MO) was examined in relation to the impact of Bi-doping of TiO_2. The doped TiO_2 with various concentrations of metal was successfully synthesized by a one-step hydrothermal method and characterized using X-ray diffraction (XRD), Fourier-transform infrared (FTIR) spectroscopy, X-ray photoelectron spectroscopy (XPS), field emission scanning electron microscopy (FESEM), and UV-vis spectroscopy. The XRD results revealed that the anatase phase, with an average crystallite size of 16.2 nm, was the main phase of TiO_2. According to the anatase texture results, it was found that the doping of TiO_2 increased the specific surface area for Bi_2O_3@TiO_2 without a change in the crystal structure or the crystal phase of TiO_2. Also, XPS analysis confirmed the formation of Ti^{4+} and Ti^{3+} as a result of doping with Bi. The activities of both pure TiO_2 and Bi-doped TiO_2 were tested to study their ability to decolorize MO dye in an aqueous solution. The photocatalytic degradation of MO over Bi_2O_3@TiO_2 reached 98.21%, which was much higher than the 42% achieved by pure TiO_2. Doping TiO_2 with Bi increased its visible-light absorption as Bi-doping generated a new intermediate energy level below the CB edge of the TiO_2 orbitals, causing a shift in the band gap from the UV to the visible region, thus enhancing its photocatalytic efficiency. In addition, the effects of the initial pH, initial pollutant concentration, and contact time were examined and discussed.

Received 15th June 2023
Accepted 8th August 2023

DOI: 10.1039/d3ra04034h

rsc.li/rsc-advances

Introduction

Owing to its potential use in the degradation of organic wastewater, the photocatalytic degradation (PCD) process is receiving significant attention from researchers throughout the world.[1–3] Titanium oxide (TiO_2) is widely utilized as a photocatalyst owing to its strong photocatalytic activity, chemical stability, favourable optoelectronic property, nontoxicity, and inexpensive cost.[4,5] Although TiO_2 generally exhibits high activity for the photocatalytic oxidation of organic pollutants, some drawbacks restrict its practical application. These drawbacks include its relatively high rate of electron–hole recombination[6,7] and its low use of the solar spectrum due to its wide bandgap (3.0–3.2 eV). Numerous techniques have been employed to increase the visible spectrum absorption capacity and lower the rate of photogenerated electron–hole recombination on the surface of TiO_2 to improve its photocatalytic effectiveness. One major method to increase the photocatalytic efficiency of TiO_2 is by doping it with various metal and non-metal components.[8–14] It has been reported that adding metal ions to TiO_2 prevents electron–hole recombination and increases its absorbance in the visible spectrum, which comprises most of the solar energy (almost 45%).[8–10]

Contrarily, Bi-based oxides are a significant family of functional materials that are extensively used in a variety of applications, including electronic ceramics, electrolytes, high-temperature superconductors, and as photoelectric conversion materials.[15,16] Bi_2O_3 stands out among these because it has certain special qualities, such as excellent electrical conductivity and a low energy bandgap (approximately 2.8 eV), which allows it to absorb visible light from the solar spectrum.[17] Hence, Bi_2O_3 has a lot of promise for use in photocatalysis. Most semiconductor compounds containing Bi have a low bandgap and effective photocatalytic activity because the hybridized $6s^2$ of Bi^{3+} and O 2p creates a new valence band that can reduce the bandgap.[18] It has been reported that Bi_2O_3 can have several crystal structures, including γ-Bi_2O_3 (1.64 eV), β-Bi_2O_3 (2.1 eV), α-Bi_2O_3 (2.8 eV), and δ-Bi_2O_3 (3.0 eV).[19] However,

[a]*Department of Chemistry, College of Science and Humanities, Prince Sattam bin Abdulaziz University, Alkharj 11942, Saudi Arabia*

[b]*Department of Chemistry, Faculty of Science, Menoufia University, Shibin El-Kom, Egypt. E-mail: elsawaf2008@yahoo.com*

[c]*Nuclear Materials Authority, El Maadi, Cairo, Egypt*

[d]*Institute of Basic and Applied Sciences, Egypt-Japan University of Science and Technology (E-JUST), Alexandria 21934, Egypt. E-mail: mohamed.elkhouly@ejust.edu.eg*

α-Bi_2O_3 is the only stable phase over a wide temperature range, while β-, δ-, and γ-Bi_2O_3 are metastable at room temperature.[20] Numerous researchers have focused on the development of bismuth-based composite oxides for use in photocatalytic hydrogen generation, water oxidation, and dye degradation. Bismuth titanate has been found to possess a high photocatalytic activity under visible light and can degrade organic pollutants and split water.[3,16]

Industrial dyestuffs constitute one of the major organic compounds (*i.e.* azo dyes) that represent a growing environmental peril.[21] Through redox reactions in aqueous media, the release of these chemicals into the environment is a significant source of hazardous pollution and can produce harmful by-products. As a result, there is increased interest in the degradation of aqueous organic dyes.[21–23] In this article, we describe a simple hydrothermal process for making nanocomposites (Bi_2O_3@TiO_2) with varying metal concentrations, as well as describe their photocatalytic activity for the degradation of methyl orange dye, which served here as a model for the degradation of organic pollutants under UV light. By eliminating the organics involved in the fabrication process by calcining the material after the hydrothermal reaction, we could improve the oxygen vacancies existing between titanium and bismuth (Ti–Bi).

Materials and methods

Chemicals

Ammonium oxalate ($C_2H_8N_2O_4$; 99.5%), sodium bismuthate ($NaBiO_3$; 90%), ascorbic acid ($HC_6H_7O_6$), titanium(III) chloride ($TiCl_3$) solution, sodium lauryl sulfate ($NaC_{12}H_{25}SO_4$), and methyl orange ($C_{14}H_{14}N_3NaO_3S$) were purchased from Sigma-Aldrich.

Fabrication of Bi_2O_3@TiO_2 photocatalyst

A porous Bi_2O_3@TiO_2 photocatalyst was synthesized *via* a hydrothermal method. Different weight portions (0.1, 0.2, or 0.3) g of sodium bismuthate were mixed well with 0.5 g of ammonium oxalate and 0.5 g of ascorbic acid in a manual mill. The previous mixture was added to 15 mL of titanium(III) chloride solution and 0.2 g sodium lauryl sulfate, and then 75 mL deionized water (DIW) was added with continuous stirring for 45 min. The gelatinous mixture formed was then transferred into a 100 mL capacity Teflon-lined stainless-steel autoclave. The autoclave was sealed and heated at 155 °C for 48 h. The precipitate was collected by filtration and washed several times with DIW and ethanol to remove the remaining and unreacted reagents. Finally, it was dried at 110 °C for 3 h in a vacuum and carefully calcined in the air at a heating rate of 2 °C min^{-1} from room temperature up to 550 °C for 180 min to obtain the Bi_2O_3@TiO_2 photocatalysts.

Characterization of the synthesized Bi_2O_3@TiO_2 composite

XRD patterns of the Bi_2O_3@TiO_2 photocatalyst powder were acquired using a PANalytical X'Pert Pro diffractometer set to 45 kV and 40 mA at 25 °C with monochromatic CuKa radiation with a wavelength of 0.15406 nm. The diffractograms were recorded with a step size of 0.013 in the scan range of 10–80°. The morphology of the produced materials was determined using a JEOL JSM scanning electron microscopy system (SEM). Elemental analysis was performed by energy-dispersive X-ray (EDX) spectrometry. Fourier transforms infrared (FTIR) spectroscopy was used to collect information on the surface chemistry of the prepared materials. The FTIR spectra were measured in the range of 500–4000 cm^{-1} on a Thermo Scientific Nicolet iS10 FTIR spectrophotometer. The surface chemical composition was investigated by X-ray photoelectron spectroscopy (XPS, UK). Also, N_2 adsorption–desorption measurements were used to determine the BET surface area and pore shape using a ChemBET Pulsar TPR/TPD system. The photocatalytic degradation was monitored using an Hitachi U-3900H double-beam UV-visible spectrophotometer in the region of 250–750 nm.

Degradation process of methyl orange

The photocatalytic activities of the Bi-doped TiO_2 samples with various Bi-doping concentrations were evaluated by the degradation of methyl orange, which is a commonly used model reaction in photocatalysis. A 350 nm UV lamp (15 W) was operated inside a black-sealed wooden box for achieving the degradation process. The degradation process was carried out using the batch method from aqueous solutions under UV light. In a typical experiment, 20 mg of each of the catalysts was added to 50 mL of 100 mg L^{-1} methyl orange aqueous solution. A magnetic stirrer operating at 400 rpm was used to mix the contents and was held inside the sealed wooden box. After shaking under UV light for an appropriate time at room temperature, the catalysts were collected by filtration. The absorption spectra of the methyl orange in aqueous solutions before and after degradation were recorded using an absorption spectrophotometer in the 250–750 nm wavelength range. The concentrations of methyl orange were calculated from the absorbance at $\lambda = 482$ nm extrapolated to a previously plotted calibration curve.

Results and discussion

Characterization of the synthesized Bi_2O_3@TiO_2 composite

The FT-IR spectrum of the Bi_2O_3@TiO_2 nanocomposite is displayed in Fig. 1a. The stretching vibration of hydroxyl functional groups (υ_{OH}), which are frequently thought to originate from the hydrothermal preparation technique, was responsible for the large peak at 3200–3600 cm^{-1}.[24,25] Because the hydroxyl radicals were produced when the terminated hydroxyl groups on the titania surface reacted with the photoinduced holes, the surface hydroxyl group contributed to the improvement of the photocatalytic activity. It has been established that titania's surface hydroxyl groups are crucial to photocatalytic reactions because they may interact with photogenerated holes to produce active oxygen species.[26] Here, the peaks located at 700 and 650 cm^{-1} were likely caused by the stretching vibrations of Bi–O and Ti–O.[24,25]

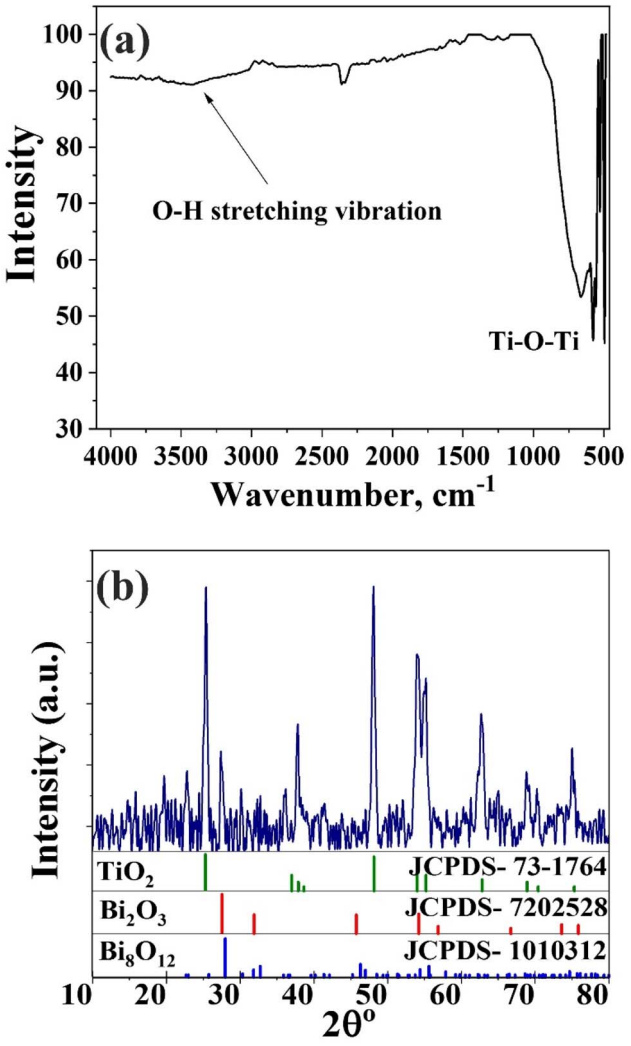

Fig. 1 (a) FTIR spectrum, and (b) XRD profiles of the prepared Bi_2O_3@TiO_2 nanocomposite.

The crystallinity of the resulting samples was characterized by XRD. The XRD pattern of the prepared Bi_2O_3@TiO_2 nanocomposite is displayed in Fig. 1b and was assigned to TiO_2 anatase (JCPDS 73-1764), Bi_2O_3 (JCPDS 7202528), and some impurities of Bi_8O_{12} (JCPDS 1010312).[27] The high intensity and narrow peaks reflected the good crystallinity of the obtained Bi_2O_3@TiO_2 composite. The main diffraction peaks of the crystalline phase at 2θ values of 25.3°, 37.8°, 48.02°, 54.02°, 55.17°, and 62.6° corresponded to the (1 0 1), (0 0 4), (2 0 0), (1 0 5), (2 1 1), and (2 0 4) crystalline planes of the anatase phase (TiO_2).[3,28] The peak of the largest intensity (101) was observed at $2\theta = 25.3°$. Other extraneous peaks in the diffraction patterns were observed for Bi_2O_3, indicating the successful synthesis of the pure Bi_2O_3@TiO_2 composite when using the hydrothermal method, Fig. 1b. The peaks at 27.3°, 31.9°,45.4°, 54.9°, and 56.8° corresponding to the (1 1 1), (0 2 0), (0 2 2), (1 3 1), and (2 2 2) planes, respectively, manifested that the Bi_2O_3 and the synthesized composite were in the form of Bi_2O_3@TiO_2 with the pure, space group $Fm\bar{3}m$, and cell parameters of $a = b = c = 5.6059$ Å, $\alpha = \beta = \gamma = 90°$, Fig. 1b.

According to Debye–Scherrer's equation, the average crystallite sizes could be determined from the XRD powder pattern (based on the broadening of the X-ray diffraction peaks). The half-width at half maximum is related to the size of crystals through the Scherrer equation: $D = k\lambda/\beta \cos\theta$[29] where D is the crystallite size, k is a constant equal to 0.89, λ is the wavelength of X-ray radiation for copper tube equal to 0.1542 nm, β is the full width at half maximum of the selected X-ray diffraction peak (the highest and largest peak), and θ is the angle of diffraction. Here, calculations were performed on the major peak. The average crystallite size for the synthesized materials was calculated by the XRD line broadening method. The calculated average crystallite size for the synthesized composite was found to be 16.2 nm (Fig. 2).

SEM analysis was used to examine the morphology of the produced Bi_2O_3@TiO_2 catalyst. Fig. 3a and b displays the SEM images of Bi_2O_3@TiO_2 at various magnifications following calcination at 550 °C. The findings support the production of porous crystallite Bi_2O_3@TiO_2 agglomerates, which were previously thought to take the form of roughly spherical nanoparticles. The existence of pores in the materials aided in increasing the light dispersion and enhancing the photocatalytic activity, which improves pollutant destruction. This makes porosity in photocatalysts a significant and desired property. The samples were also looked at using a SEM system that had an EDX (energy-dispersive X-ray spectroscopy) unit attached to it. Fig. 3c–f shows the Ti, Bi, and O elemental mapping results for the Bi-doped TiO_2 photocatalyst; whereby a uniform dispersion of the three elements could be seen in this sample with a Bi-doping level of 1.12 wt%.

Understanding the mechanism of adsorption, which depends on the pores and surface structure, is crucial. Whether physical, chemical, or solid, porous conditions all affect the isotherm shape. The BET method was employed to establish the photocatalyst's textural characteristics, and nitrogen adsorption was used to ascertain some structural information. The adsorption–desorption isotherm of the Bi_2O_3@TiO_2 nanocomposite at 77 K is given in Fig. 4a. According to the IUPAC classification, the adsorption and desorption isotherm obtained

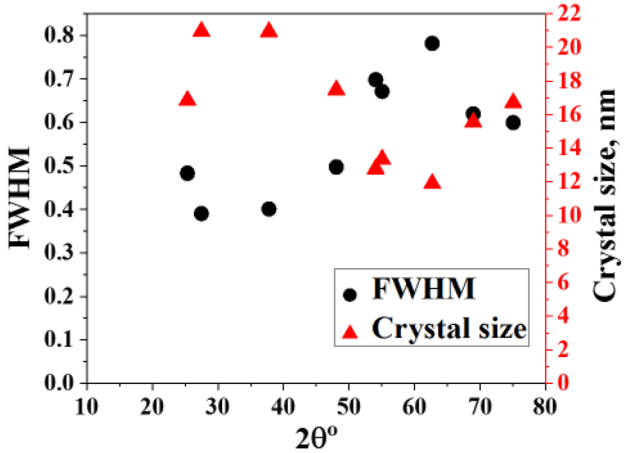

Fig. 2 Crystal size of the synthesized Bi_2O_3@TiO_2 nanocomposite.

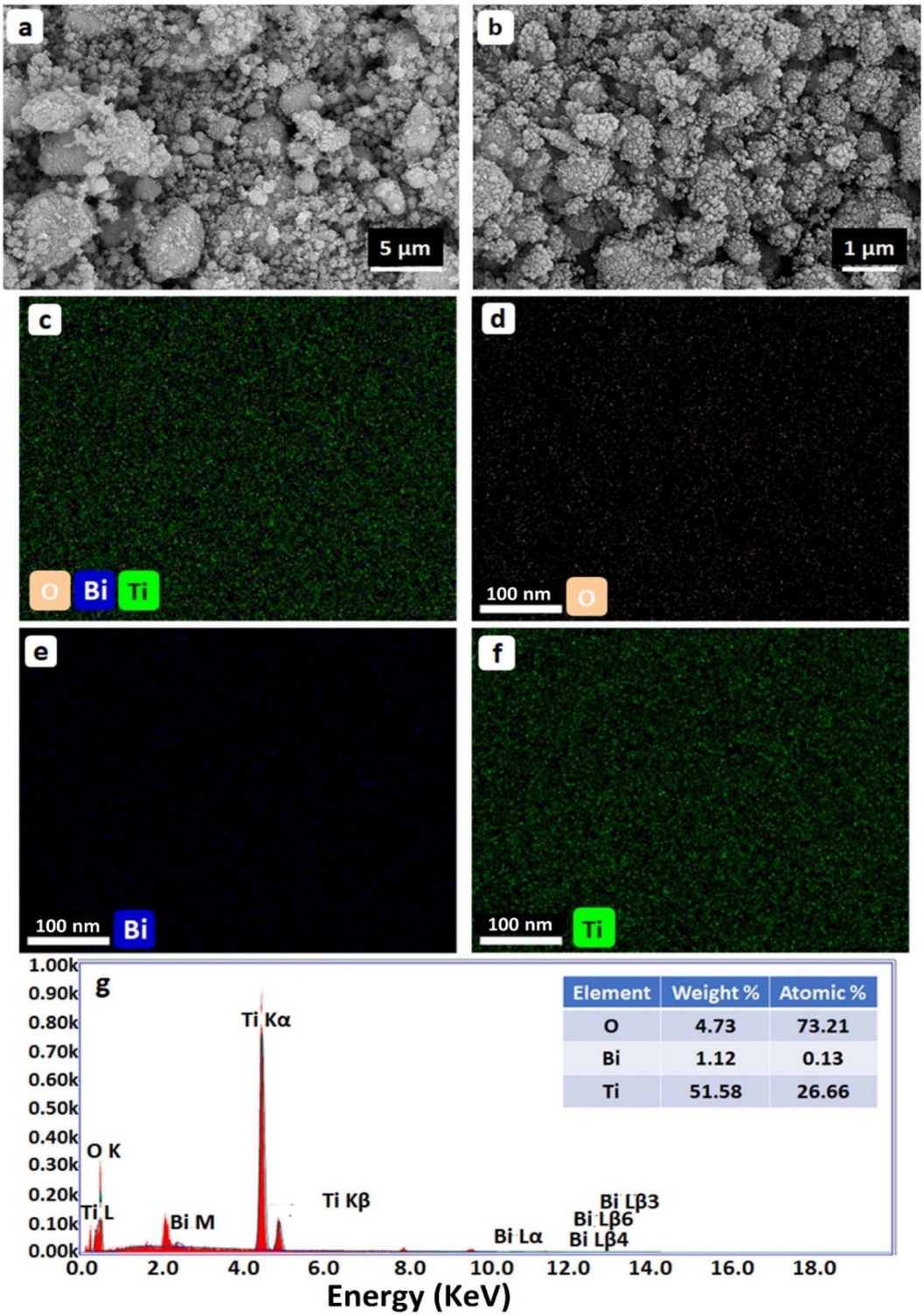

Fig. 3 (a and b) SEM images with different magnifications, (c–f) elemental mapping results, and (g) EDX spectrum of Bi doped TiO_2 NPs.

could be classified as Type IV with an H3-hysteresis loop.[30,31] Type IV isotherms are obtained with mesoporous (2 nm < pore size < 50 nm) solids. These are characterized by a hysteresis loop and a saturation plateau at $P/P_0 < 1$. The hysteresis loop in the isotherm was due to filling the mesopores *via* a different mechanism of multilayer formation followed by capillary condensation. The shapes of hysteresis loops have often been correlated to specific pore morphologies and the textural properties of the adsorbent.[31,32] Type H3 hysteresis is usually found in materials with a wide distribution of pore sizes. In

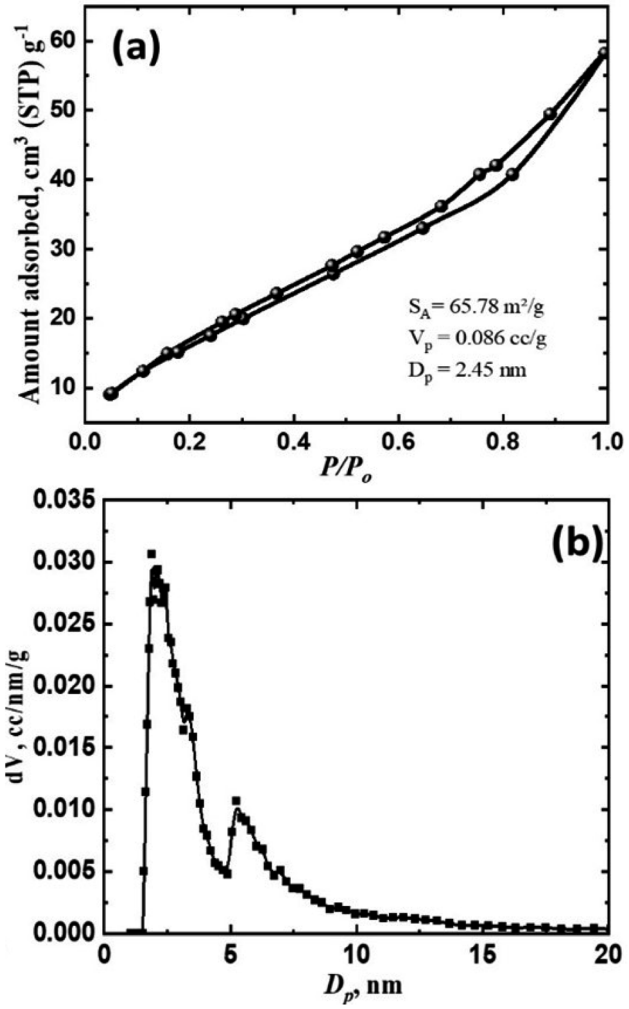

Fig. 4 Nitrogen adsorption/desorption isotherm (a) and pore-size distribution (b) of the synthesized Bi_2O_3@TiO_2 nanocomposite.

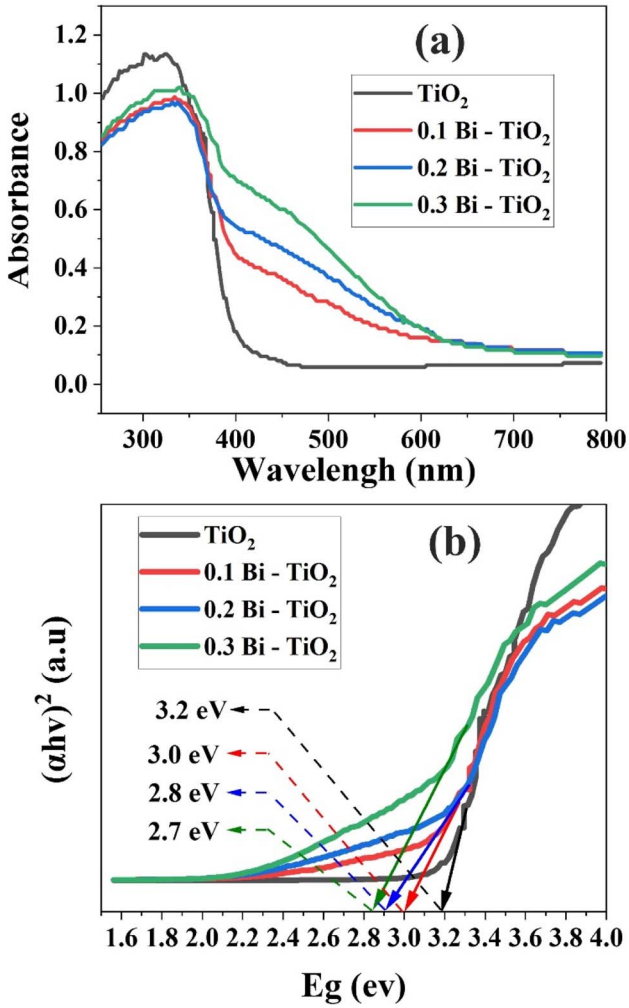

Fig. 5 (a) Ultraviolet-visible (UV-vis) diffuse reflectance spectra of the investigated samples. (b) Bandgap values ascertained through Tauc plot.

addition, it was observed that aggregates of plate-like particles give rise to slit-shaped pores. Thus, it can be concluded that there was a multilayer range of physisorption isotherms here because of the porous structure with nanochannels between the oxide particles. The pore-size distribution was calculated from the corresponding desorption isotherms plot by using the Barrett–Joyner–Halenda (BJH) method, indicating that these Bi_2O_3@TiO_2 nanoparticles had a very pronounced mesoporous structure (Fig. 4b). The calculated BET-specific surface area and pore diameter of Bi_2O_3@TiO_2 were 65.78 m^2 g^{-1} and 2.45 nm, respectively.

The presented results demonstrate that there were notable changes in the optical properties of the Bi_2O_3@TiO_2 catalysts compared to pure TiO_2. Fig. 5a illustrates the UV-vis diffuse reflectance spectra, revealing a red-shift in the absorption curves of Bi_2O_3@TiO_2. This shift indicated a significant enhancement in the catalyst's ability to absorb visible light within the range of 400–600 nm.[18] The introduction of Bi facilitated the coexistence of Bi electrons and the conduction band (CB) electrons of TiO_2, thereby enabling charge-transfer transitions between them.

To determine the bandgap energy, a Tauc plot was employed, which involved graphing $(\alpha h\nu)^2$ against $h\nu$, where α is the absorption coefficient, h is Planck's constant, ν denotes the frequency of incident light, and E represents the energy.[3] Fig. 5b illustrates the bandgap energies of TiO_2, 0.1 Bi–TiO_2, 0.2 Bi–TiO_2, and 0.3 Bi–TiO_2 were 3.2, 3.0, 2.8, 2.7, and 2.7 eV, respectively. These outcomes signified that the introduction of Bi as a dopant caused a noticeable reduction in the bandgap of TiO_2, ultimately enhancing its absorption capabilities in the visible region.

The chemical states of the elements in the undoped and Bi_2O_3-doped TiO_2 nanoparticles were examined by XPS analysis. Fig. 6a shows the XPS survey spectrum of a Bi_2O_3-doped TiO_2 sample, demonstrating the presence of Bi, Ti, and O in the sample. As illustrated in Fig. 6b, the Ti_2p high-resolution spectrum of Bi_2O_3-doped TiO_2 nanoparticles revealed two distinct peaks at 458.57 and 464.3 eV, assigned to the Ti $2p_{3/2}$ and Ti $2p_{1/2}$ orbitals of Ti^{4+} (TiO_2), respectively.[33,34] Moreover, the peak separation of 5.7 eV between these two Ti 2p doublets

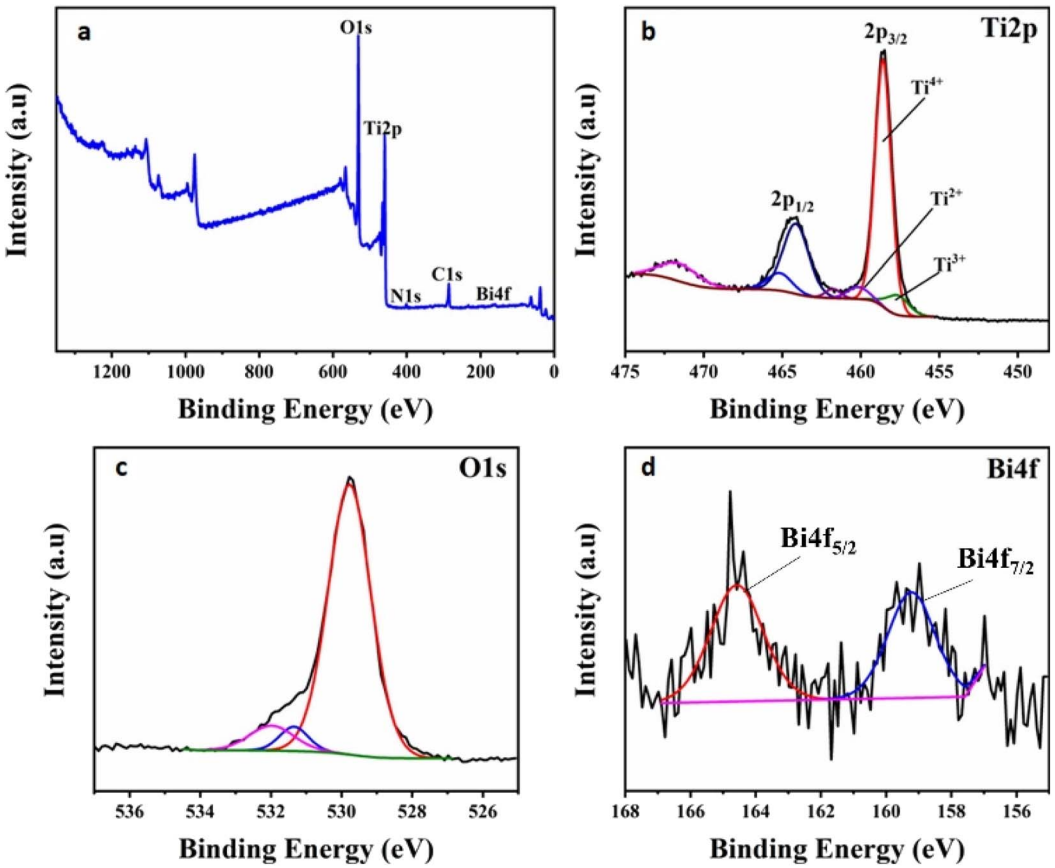

Fig. 6 (a) XPS survey spectrum of the Bi_2O_3-doped TiO_2 nanocomposite. XPS spectra of (b) Ti 2p, (c) O 1s, and (d) Bi 4f core levels measured for the Bi_2O_3-doped TiO_2 nanocomposite.

indicated the existence of Ti^{4+} ions in the TiO_2 lattice.[35–38] Besides the peaks of Ti^{4+} ions, less intense peaks were also observed corresponding to a small content of Ti^{2+} and Ti^{3+} ions. This finding infers that the oxidation state of Ti was reduced with the Bi replacement.[39] The O 1s region in the Bi_2O_3-doped TiO_2 sample displayed three peaks, as shown in Fig. 6c. The peak centred at 529.77 eV was ascribed to the Ti–O in TiO_2.[39] The second peak, located at 531.33 eV, was attributed to the oxygen connected to the bismuth (Bi–O bond of bismuth oxide);[39] whereas the third peak at 531.9 eV was associated with surface OH^- groups.[40] In the Bi 4f high-resolution spectrum of the Bi_2O_3-doped TiO_2 sample (Fig. 6d), two major peaks centred at binding energies of 159.23 and 164.58 eV could be observed, corresponding well to the Bi $4f_{7/2}$ and Bi $4f_{5/2}$ peaks of Bi^{3+} species.[33,34,41–43] These peaks were recorded with a relatively low signal-to-noise ratio because of the low Bi-doping content. The split of 5.3 eV between the Bi 4f doublets confirmed the Bi^{3+} valence state and Bi_2O_3 structure in the prepared catalyst.[34] For comparison, the XPS analyses of pure α-Bi_2O_3 mentioned in previous studies[33,40,42] were used. The binding energy of the Bi $4f_{7/2}$ and Bi $4f_{5/2}$ peaks of pure α-Bi_2O_3 were 158.6 and 163.9 eV, respectively. It is interesting to note that the peaks of Bi 4f in the doped sample were shifted to a higher binding energy. Reddy *et al.*[42] assigned this positive shift to the partial oxidation of Bi^{3+} to the $Bi^{(3+\delta+)}$ state obtained with a quite low Bi-doping content. Furthermore, this binding energy enhancement could be attributed to the Bi–O–Ti bond formation in the titania framework.[39]

Photocatalytic activity of the synthesized Bi_2O_3@TiO_2 nanocomposite

The degradation of MO in aqueous solution under UV-light irradiation was used to test the photocatalytic activity of the produced Bi_2O_3@TiO_2 nanocomposite. For the UV-vis absorption investigations, aqueous solutions of pure and Bi-doped TiO_2 nanopowders were employed. Fig. 7 depicts the altered absorption spectra after UV radiation (λ_{max} = 482 nm) was applied to MO (500 mg L^{-1}) in the presence of pure undoped TiO_2 and the Bi_2O_3@TiO_2 nanoparticles (10 mg) as the photocatalyst. Due to the dye's decolorization after UV-light irradiation, the strength of absorption decreased. The fluorescence quenching effectiveness of MO in the presence of the Bi_2O_3@-TiO_2 nanoparticles is depicted in Fig. 6 in the insets as a function of UV light. The results revealed that the photocatalytic activity of the Bi-doped TiO_2 catalysts decreased in the following order: (0.3 g Bi)–TiO_2 < (0.1 g Bi)–TiO_2 < (0.2 g Bi)–TiO_2, whereby the TiO_2 sample doped with 0.2 g of Bi showed the highest efficiency. No degradation of the dye was observed in the dark, which proved that no acute adsorption of MO on the surface of

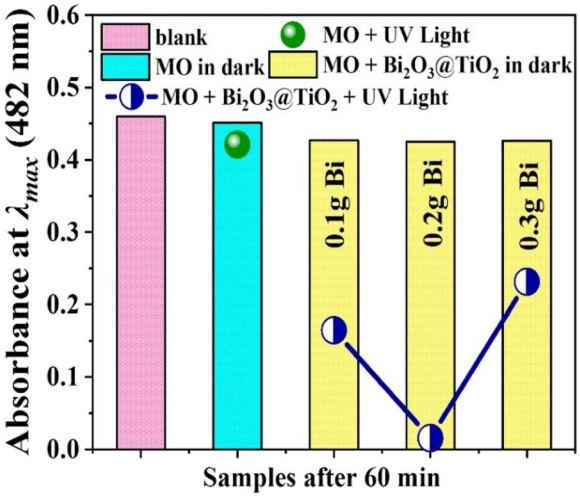

Fig. 7 Absorption spectra during the degradation process of MO dye at λ_{max} = 482 nm.

the prepared catalysts was detected, implying that the decolorization was primarily caused by photocatalytic degradation rather than physiochemical adsorption on the surface of the nanostructured hybrid (Fig. 7). Moreover, in the absence of a catalyst, less than 0.5% of MO was degraded after 30 min under UV irradiation, demonstrating that MO has high photostability under UV-light irradiation and that the autodegradation of MO can be ignored (Fig. 7). In addition, the photocatalytic performance was compared with pure TiO_2, and the results showed that the photocatalytic activity of the TiO_2 catalyst was highly enhanced by Bi-doping. With Bi-doping, a new energy level was introduced into the forbidden bandgap below the conduction band (CB) edge of TiO_2, which expanded the absorption to the visible-light region and acted as an electron–hole generator.[26] Moreover, the high surface area of the prepared Bi-doped TiO_2 is beneficial for readsorption and contact between photogenerated carriers and the reactants.

Since photocatalysis takes place on the catalyst surface, the pH is a crucial parameter for the photocatalytic degradation of wastewater and dyes.[45,46] To accurately forecast the charge on the NPs surface throughout the photodegradation process, the point of zero charge (pH_{PZC}) must be identified.[44–46] The performance of the photocatalyst is remarkably influenced by the solution pH as it affects the surface's ability to adsorb pollutants. We thus evaluated the zeta potentials of the prepared photocatalyst at different pH levels to determine the influence of the pH on the degradation rate of MO. The point of zero charges (pzc) of Bi_2O_3@TiO_2 was measured as shown in Fig. 8a to be at pH 7.5. The higher pzc values of the Bi-doped TiO_2 compared to the pzc of pure TiO_2 (pH 6.5 in the literature[44]) could be attributed to the presence of the surface OH groups, which was consistent with the IR spectra. The surface of the synthesized photocatalyst became positive when the pH of the solution was less than the pH_{PZC} value of the catalyst, and negative when the pH of the solution was more than the pH_{PZC} value.

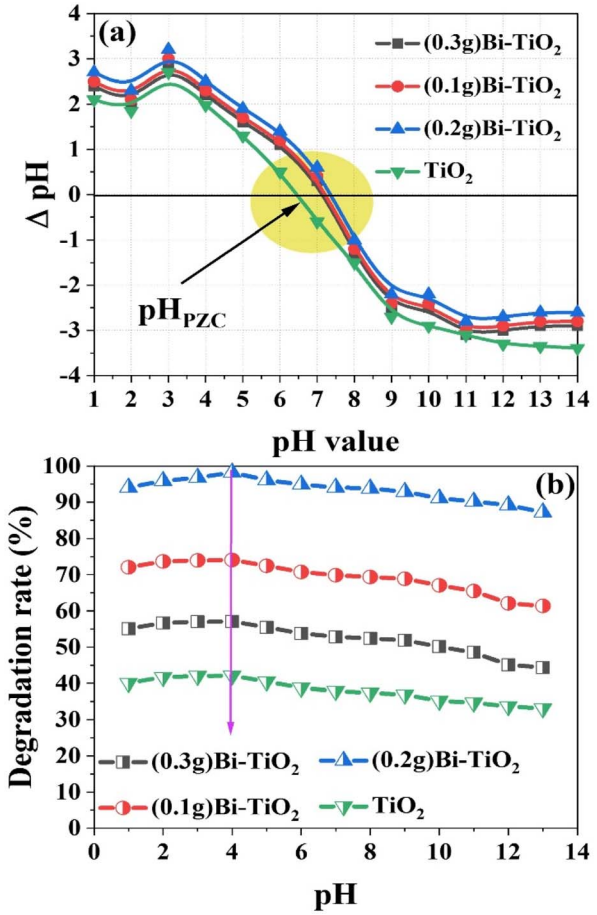

Fig. 8 (a) pH_{PZC} of Bi_2O_3@TiO_2 catalysts in 0.01 M KCl as a function of pH. (b) Effect of the pH on the degradation of MO using the synthesized Bi_2O_3@TiO_2 photocatalysts under the optimal condition.

The effect of pH on the rate of MO dye photocatalytic degradation is depicted in Fig. 8b. Under the influence of UV light, a fixed weight of the synthesized photocatalysts (10 mg) and a 10 mL solution volume of 50 mg L^{-1} MO at room temperature were utilized. The highest degradation efficiency was recorded in acidic solutions with a pH of 4, whereas the degradation was lower in alkaline pH solutions after 60 min of contact time. The impact of the pH is typically attributed to the catalyst's surface charge and how it interacts with the ionic form of organic components. Methyl orange (MO) is an anionic azo dye with sulfonate groups that are negatively charged. As a result, under acidic conditions, the surface of Bi-doped TiO_2 gains a positive charge. This causes more dye to bind to a positively charged catalyst surface, speeding up the rate at which the acidic media degrades the catalyst. Additionally, methyl orange occurs in a quinonoid form in acidic medium, and the rate of degradation can be further accelerated in the absence of a stable azo ink.[47] Under contrast, negatively charged catalyst surfaces tend to resist the adsorption of anionic adsorbate species under an alkaline state, reducing the amount of dye adsorbed on the surface and impeding the photocatalytic reaction.

The doping of TiO_2 with Bi_2O_3 was aimed at enhancing its photocatalytic activity. However, an excessive amount of Bi_2O_3 incorporation can lead to various effects. First, it can cause a reduction in surface area. When too much Bi_2O_3 is added, particles tend to aggregate, resulting in a decrease in the available surface area for dye adsorption and photocatalytic reactions. This leads to a reduced interaction between the dye molecules and the catalyst, ultimately resulting in a decrease in the degradation efficiency. Second, an increased amount of Bi_2O_3 doping can introduce additional charge carriers, like electrons and holes, to the TiO_2 catalyst. While this can be advantageous, excessive Bi_2O_3 can actually lead to an increase in charge recombination. This refers to the phenomenon where the photogenerated electrons and holes recombine before participating in degradation reactions. As a result, the overall efficiency of the catalyst in breaking down dye molecules decreases. Supporting these findings, the results here indicated that different amounts of Bi_2O_3 doping had varying impacts on the degradation of dye molecules. According to Fig. 9a, within the first 15 min of contact time, (0.3 g Bi)–TiO_2, (0.1 g Bi)–TiO_2, and (0.2 g Bi)–TiO_2 degraded 26.1%, 35.3%, and 46.45% of the dye, respectively. However, after 60 min, (0.2 g Bi)–TiO_2 displayed the highest efficiency at 98.21%, while (0.3 g Bi)–TiO_2 and (0.1 g Bi)–TiO_2 exhibited efficiencies of 57.1% and 77.1% respectively.

The reaction kinetics was addressed to understand the photocatalytic degradation behaviour of MO dye using Bi-doped TiO_2. The bleaching reaction follows a pseudo-first-order reaction kinetics for the photocatalytic oxidation process. The pseudo-first-order model ($\ln(C/C_o) = -Kt$) governs the photocatalytic degradation of most organic contaminants at the liquid–solid interface, as is well known;[48] where C_0 represents the initial concentration of MO; C represents the concentration of MO at time t, and k is the rate constant (min^{-1}). Here, 50 mL of MO (500 mg L^{-1}) was combined with 50 mg portions of each of (0.1 g Bi)–TiO_2, (0.2 g Bi)–TiO_2, and (0.3 g Bi)–TiO_2 at different time intervals under the impact of UV irradiation. The correlation constant for the fitted line was calculated to be $R^2 > 0.98$ for the doped TiO_2 (0.1 g Bi)–TiO_2, (0.2 g Bi)–TiO_2, and (0.3 g Bi)–TiO_2, indicating that the photocatalytic degradation process well-fitted with the pseudo-first-order kinetic model. A straight line with a slope was generated from the linear correlation between ln (C/C_o) and t (Fig. 9(b–d)), and was used to get the values of K (Table 1). At pH 4, the apparent reaction rate constant of (0.2 g Bi)–TiO_2 was 6.88×10^{-2} min^{-1}, while for (0.1 g Bi)–TiO_2 and (0.3 g Bi)–TiO_2, lower reaction rates of 2.47×10^{-2} and 1.47×10^{-2} min^{-1} were detected. The effectiveness of the photocatalytic degradation process was significantly influenced by

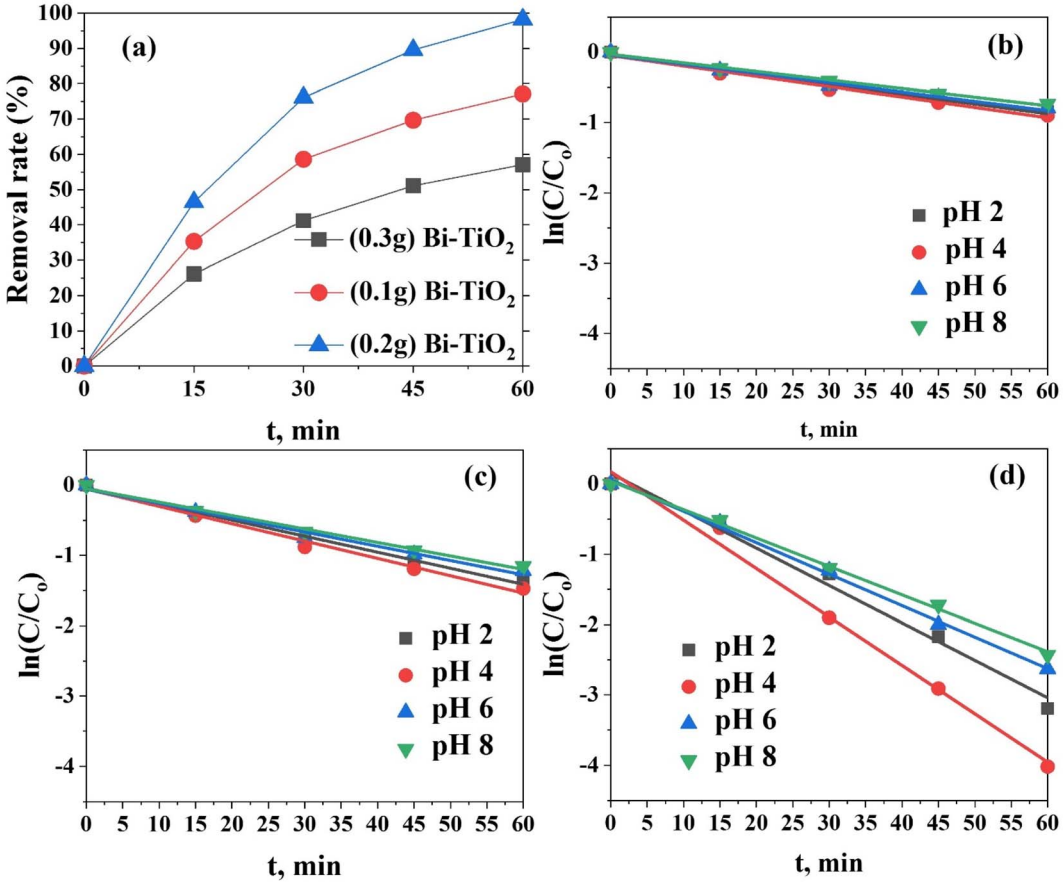

Fig. 9 (a) Removal efficiency of the synthesized photocatalysts, (b–d) pseudo-first-order kinetics of the photodegradation of MO using (0.3 g Bi)–TiO_2, (0.1 g Bi)–TiO_2, and (0.2 g Bi)–TiO_2 photocatalysts at different pH values.

Table 1 Pseudo-first-order kinetic model of the photodegradation of MO using (0.3 g Bi)–TiO_2, (0.2 g Bi)–TiO_2, and (0.1 g Bi)–TiO_2 photocatalysts at different pH values

		(0.3 g Bi)–TiO_2	(0.1 g Bi)–TiO_2	(0.2 g Bi)–TiO_2
pH 2	R^2	0.9878	0.9902	0.9872
	K	1.38×10^{-2}	2.28×10^{-2}	5.31×10^{-2}
pH 4	R^2	0.9870	0.9890	0.9916
	K	1.47×10^{-2}	2.47×10^{-2}	6.88×10^{-2}
pH 6	R^2	0.9868	0.9847	0.9974
	K	1.31×10^{-2}	2.03×10^{-2}	4.47×10^{-2}
pH 8	R^2	0.9917	0.9904	0.9973
	K	1.21×10^{-2}	1.91×10^{-2}	4.04×10^{-2}

the impact of the initial MO concentrations on the photocatalytic behaviour of Bi-doped TiO_2.[49,50]

Assessment for the effect of the initial concentration of MO on photocatalytic decolonization was carried out at a fixed amount of the (0.2 g Bi)–TiO_2 sample (50 mg L^{-1})) and with varying the concentration of the dye ((*i.e.*, 2, 20, 50, 200, 500, and 1000 mg L^{-1}) under optimal operating conditions in a single solution system (*i.e.*, pH 4, contact time 60 min at 25 °C). The photocatalytic degradation gradually declined as the initial dye concentration was increased beyond 500 mg L^{-1}. Approximately 100% dye degradation of 500 mg L^{-1} dye was observed after 30 min contact time, while only 82.1% dye was degraded in 60 min with 1000 mg L^{-1} dye solution (Fig. 10). Because there were more MO molecules present and there was a fixed number of active catalyst sites, the rate of photocatalysis was reduced as the concentration of MO dye increased. A high initial dye concentration caused many layers of adsorbed dye molecules to develop on the catalyst surface, which prevented light from coming into direct contact with the catalyst and producing hydroxyl radicals, thus slowing down the rate of degradation.[49–55]

One of the key markers of a photocatalyst's usefulness and practical benefits is its stability.[50,51] To assess the economic viability of the photocatalytic degradation process, the number of times the photocatalyst can be reused was obtained. The durability and stability of the Bi_2O_3@TiO_2 (0.2 g Bi) photocatalyst were investigated as shown in Fig. 11, where it can be seen the efficiency of the Bi_2O_3@TiO_2 photocatalyst was only reduced from 98.21% to 91.18% after 6 degradation cycles, demonstrating that the Bi_2O_3@TiO_2 photocatalyst had good stability against repeated usage. The main cause for the decrease in efficiency was the presence of degradation by-products formed at the Bi_2O_3@TiO_2 surface, which decreased the number of adsorption sites. It can be concluded from these results that the catalyst Bi_2O_3@TiO_2 can be efficiently employed in the MO-degradation process with minor efficiency losses and great durability.

To ensure the durability and stability of the Bi_2O_3@TiO_2 photocatalyst throughout 6 consecutive cycles of dye degradation, the material was subjected to elution using 0.1 M hydrochloric acid, followed by a thorough rinsing with water.

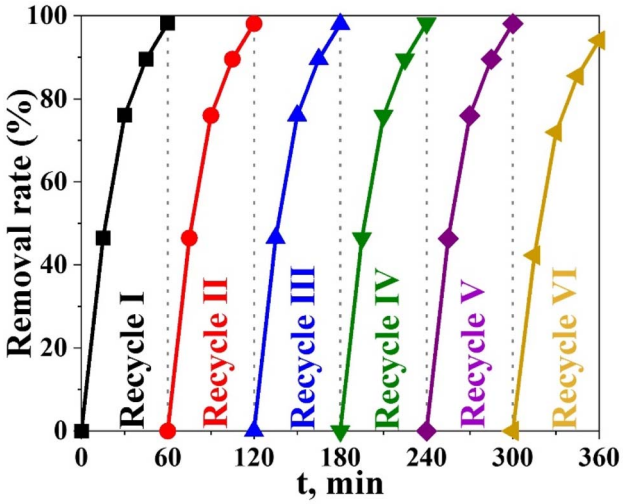

Fig. 11 Reusability studies of the (0.2 g Bi)–TiO_2 photocatalyst.

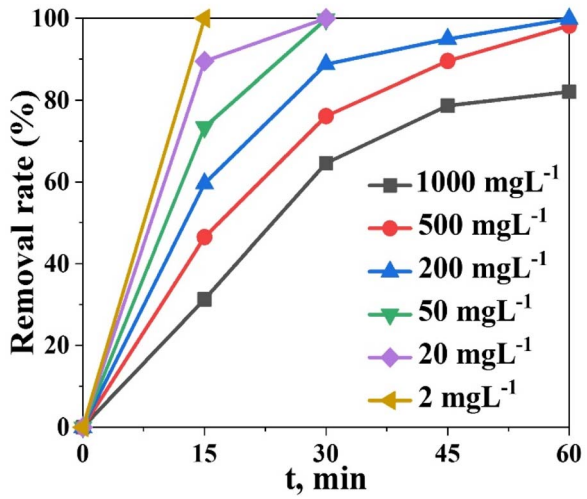

Fig. 10 Degradation efficiency (%) of the (0.2 g Bi)–TiO_2 photocatalyst as a function of the initial concentration at pH 4.

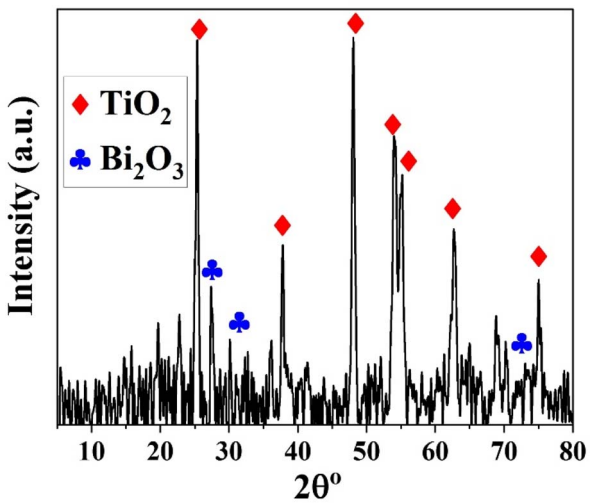

Fig. 12 XRD profiles after 6 consecutive cycles of the degradation process.

Subsequently, the material was air-dried and subjected to XRD analysis. The XRD results, as depicted in Fig. 12, exhibited the presence of titanium oxide in the anatase phase, along with the bismuth oxide phase (Bi_2O_3). This outcome indicates that the synthesized catalyst, Bi_2O_3@TiO_2, maintained its crystalline structure and overall stability, even after undergoing 6 consecutive cycles of dye deterioration under irradiation.

Photocatalytic degradation mechanism

The degradation mechanism of methyl orange dye using the Bi_2O_3@TiO_2 photocatalyst under UV light involved a series of photophysical and photochemical processes (Fig. 13). The presence of Bi_2O_3 in conjunction with the anatase phase of TiO_2 greatly influenced the overall efficiency of the photocatalytic degradation. Upon exposure to UV light, the photocatalyst absorbed photons, leading to the excitation of electrons from the valence band (VB) to the conduction band (CB) of TiO_2. In the presence of Bi_2O_3, the electrons and holes generated in this process were effectively separated due to the heterojunction formed between the TiO_2 (anatase) and Bi_2O_3 phases. This separation minimized the recombination of electron–hole pairs, allowing for the enhanced photocatalytic activity.

The degradation of methyl orange dye occurred through two main pathways: direct and indirect mechanisms. In the direct mechanism, the excited electrons in the conduction band of the photocatalyst react with adsorbed O_2 to generate superoxide radicals ($^{\bullet}O_2^-$). These radicals, being highly reactive, can directly oxidize the methyl orange dye molecules, initiating the degradation process. This direct pathway is represented by the following equation:

$$TiO_2\ (CB) + O_2 \rightarrow TiO_2\ (VB) + {}^{\bullet}O_2^-$$

In the indirect mechanism, the photoexcited electrons in the conduction band of TiO_2 can transfer to the surface of Bi_2O_3, where they react with adsorbed water molecules, generating hydroxyl radicals ($^{\bullet}OH$). These hydroxyl radicals play a vital role in oxidizing the methyl orange dye and breaking down its chemical structure. The indirect pathway can be represented by the following equations:

$$TiO_2\ (CB) + H_2O \rightarrow TiO_2\ (VB) + {}^{\bullet}OH$$

$$^{\bullet}OH + \text{Methyl Orange} \rightarrow \text{Degradation Products}$$

The presence of Bi_2O_3 in the photocatalyst promoted the formation of hydroxyl radicals by facilitating the transfer of electrons from TiO_2 to Bi_2O_3. As a result, the rate of methyl orange dye degradation was significantly enhanced. The doping of Bi_2O_3 also improved the stability and reusability of the TiO_2 photocatalyst, making it a promising material for efficient dye degradation applications.

Conclusions

In this study, mesoporous Bi-doped TiO_2 catalysts were successfully synthesized, and their photocatalytic degradation activity was examined using MO dye. Various analytical and spectroscopic methods were used to confirm the production and crystallinity of the synthesized catalytic composites. When compared to undoped TiO_2, the produced catalysts loaded with Bi_2O_3 displayed a high photocatalytic activity under UV light. Bi-doping had two impacts on TiO_2, including occupying the electron–hole recombination sites and increasing the catalyst's absorption wavelength range into the visible area. After 60 min of exposure, the (0.2 g Bi)–TiO_2 sample displayed the maximum activity in the photocatalytic degradation of MO, with an efficiency of 98.21%. The pseudo-first-order model was compatible with the catalytic degradation mechanism. The synthesized catalyst also showed remarkable recycling properties for up to six times use. The newly created Bi_2O_3@TiO_2 composites could therefore be used as a viable and beneficial photocatalyst for the elimination of organic pollutants from industrial and wastewater.

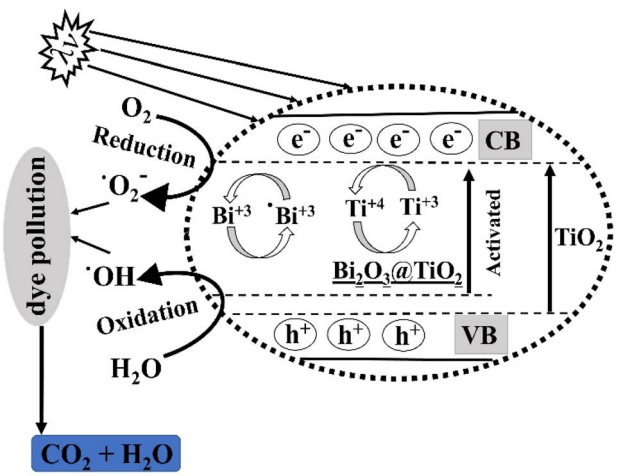

Fig. 13 Photocatalytic degradation mechanism.

Author contributions

Dina Tolan: conceptualization, methodology, writing – original draft. Ayman El-Sawaf: data curation, writing – review & editing, supervision. Islam Alhindawy: data analysis, methodology, writing – original draft. Mohammed Ismael: data analysis, investigation, visualization, Amal Nassar: data curation, methodology, visualization. Ahmed El-Nahas: writing, review, editing, supervision. Mai Maize: conceptualization, supervision, writing – review & editing. Emad Elshehy: visualization, investigation, writing – review & editing. Mohamed E. El-Khouly: visualization, data analysis, writing, editing, revision.

Conflicts of interest

There are no conflicts to declare.

Acknowledgements

The authors extend their appreciation to the Deputyship for Research & Innovation, Ministry of Education in Saudi Arabia for funding this research work through the project number (IF-PSAU-2021/01/18797).

References

1 C. Pan, J. Xu, Y. J. Wang, D. Li and Y. Zhu, Dramatic Activity of C_3N_4/$BiPO_4$ Photocatalyst with Core/Shell Structure Formed by Self-Assembly, *Adv. Funct. Mater.*, 2012, **22**, 1518.

2 J. Chen, W. Mei, C. Liu, C. Hu, Q. Huang, N. Chen, J. Chen, R. Zhang and W. Hou, Carbon-modified bismuth titanate with enhanced photocatalytic activity under nature sunlight, *Mater. Lett.*, 2016, **172**, 184.

3 I. Alhindawy, E. Elshehy, A. Youssef, S. Abdelwahab, A. Zaher, W. El-Said, H. Mira and A. Abdelkader, Improving the photocatalytic performance of cobalt-doped titania nanosheets by induced oxygen vacancies for efficient degradation of organic pollutants, *Nano-Struct. Nano-Objects*, 2022, **31**, 100888.

4 I. Alhindawy, H. Mira, A. Youssef, S. Abdelwahab, A. Zaher, W. A. El-Said, E. Elshehy and A. Abdelkader, Cobalt doped titania-carbon nanosheets with induced oxygen vacancies for photocatalytic degradation of uranium complexes in radioactive wastes, *Nanoscale Adv.*, 2022, **4**, 5330.

5 J. Herrmann, Heterogeneous photocatalysis: fundamentals and applications to the removal of various types of aqueous pollutants, *Catal. Today*, 1999, **53**, 115.

6 X. Yu, B. Kim and Y. Kim, Highly Enhanced Photoactivity of Anatase TiO_2 Nanocrystals by Controlled Hydrogenation-Induced Surface Defects, *ACS Catal.*, 2013, **3**, 2479.

7 H. Zabihi-Mobarakeh and A. Nezamzadeh-Ejhieh, Application of supported TiO_2 onto Iranian clinoptilolite nanoparticles in the photodegradation of mixture of aniline and 2,4-dinitroaniline aqueous solution, *J. Ind. Eng. Chem.*, 2015, **26**, 315.

8 T. Pham and B. Lee, Novel adsorption and photocatalytic oxidation for removal of gaseous toluene by V-doped TiO_2/PU under visible light, *J. Hazard. Mater.*, 2015, **300**, 493.

9 M. Pelaez, N. T. Nolan, S. C. Pillai, M. K. Seery, P. Falaras, A. G. Kontos, P. S. M. Dunlop, J. W. J. Hamilton, J. A. Byrne, K. O'Shea, M. H. Entezari and D. D. Dionysiou, A review on the visible light active titanium dioxide photocatalysts for environmental applications, *Appl. Catal., B*, 2012, **125**, 331–349.

10 J. Xua, M. Chena and D. Fub, Study on highly visible light active Bi-doped TiO_2 composite hollow sphere, *Appl. Surf. Sci.*, 2011, **257**, 7381.

11 H. Li, J. Liu, J. Qian, Q. Li and J. Yang, Preparation of Bi-doped TiO_2 nanoparticles and their visible light photocatalytic performance, *Chin. J. Catal.*, 2014, **35**, 1578.

12 R. Asahi, T. Morikawa, T. Ohwaki, K. Aoki and Y. Taga, Visible-light photocatalysis in nitrogen-doped titanium oxides, *Science*, 2001, **293**, 269.

13 W. J. Ren, Z. H. Ai, F. L. Jia, L. Z. Zhang, X. X. Fan and Z. G. Zou, Low temperature preparation and visible light photocatalytic activity of mesoporous carbon-doped crystalline TiO_2, *Appl. Catal., B*, 2007, **59**, 138.

14 G. Liu, Y. N. Zhao, C. H. Sun, F. Li, G. Q. Lu and H. M. Cheng, Synergistic Effects of B/N Doping on the Visible-Light Photocatalytic Activity of Mesoporous TiO_2, *Angew. Chem., Int. Ed.*, 2008, **47**, 4516.

15 W. Yi, C. Yan, M. S. Hamdy, J. Baltrusaitis and G. Mul, Effects of bismuth addition and photo-deposition of platinum on (surface) composition, morphology and visible light photocatalytic activity of sol-gel derived TiO_2, *Appl. Catal., B*, 2014, **153**, 154–155.

16 Y. Chen, D. Chen, J. Chen, Q. Lu, M. Zhang, B. Liu, Q. Wang and Z. Wang, Facile synthesis of Bi nanoparticle modified TiO_2 with enhanced visible light photocatalytic activity, *J. Alloys Compd.*, 2015, **651**, 114–120.

17 H. Cheng, B. Huang and Y. Dai, Engineering BiOX (X = Cl, Br, I) nanostructures for highly efficient photocatalytic applications, *Nanoscale*, 2014, **6**, 2009.

18 Z. Chen, H. Jiang, W. Jin and C. Shi, Enhanced photocatalytic performance over $Bi_4Ti_3O_{12}$ nanosheets with controllable size and exposed {0 0 1} facets for Rhodamine B degradation, *Appl. Catal., B*, 2016, **180**, 698.

19 S. Chen, Y. Li, R. Lu and P. Wang, Preparation, characterization of C/Fe-Bi_2WO_6 nanosheet composite and degradation application of norfloxacin in water, *J. Nanosci. Nanotechnol.*, 2013, **13**, 5624.

20 Z. Chen, J. Liang, X. Xu, G. He and H. Chen, CdS-Bi_2MoO_6/RGO nanocomposites for efficient degradation of ciprofloxacin under visible light, *J. Mater. Sci.*, 2020, **55**, 6065.

21 I. Konstantinou and T. Albanis, TiO_2-assisted photocatalytic degradation of azo dyes in aqueous solution: kinetic and mechanistic investigations: a review, *Appl. Catal., B*, 2004, **49**, 1.

22 A. Bianco-Prevot, C. Baiocchi, M. C. Brussino, E. Pramauro, P. Savarino, V. Augugliaro, G. Marci and L. Palmisano, Photocatalytic Degradation of Acid Blue 80 in Aqueous Solutions Containing TiO_2 Suspensions, *Environ. Sci. Technol.*, 2001, **35**, 971.

23 B. Neppolian, H. C. Choi, S. Sakthivel, B. Arabindoo and V. Murugesan, Solar light-induced and TiO_2 assisted degradation of textile dye reactive blue 4, *Chemosphere*, 2002, **46**, 1173.

24 K. M. Khalil and M. I. Zaki, Photocatalytic Degradation of Acid Blue 80 in Aqueous Solutions Containing TiO_2 Suspensions, *Powder Technol.*, 1997, **92**, 233–239.

25 G. Colon, M. Maicu, M. C. Hidalgo and J. A. Navio, Cu-doped TiO_2 systems with improved photocatalytic activity, *Appl. Catal., B*, 2006, **67**, 41–51.

26 P. Rychtowski, B. Tryba, A. Skrzypska, P. Felczak, J. Srenscek-Nazzal, R. J. Wróbel, H. Nishiguchi and M. Toyoda, Role of the Hydroxyl Groups Coordinated to TiO_2 Surface on the Photocatalytic Decomposition of Ethylene at Different Ambient Conditions, *Catalysts*, 2022, **12**, 386.

27 J.-J. Li, S.-C. Cai, Z. Xu, X. Chen, J. Chen, H.-P. Jia and J. Chen, Solvothermal syntheses of Bi and Zn co-doped TiO_2 with enhanced electron-hole separation and efficient photodegradation of gaseous toluene under visible-light, *J. Hazard. Mater.*, 2017, **325**, 261.

28 B. Benalioua, M. Mansour, A. Bentouami, B. Boury and E. Elandaloussi, The layered double hydroxide route to Bi-Zn co-doped TiO_2 with high photocatalytic activity under visible light, *J. Hazard. Mater.*, 2015, **288**, 158.

29 I. G. Alhindawy, M. I. Sayyed, A. H. Almuqrin and K. A. Mahmoud, Optimizing gamma radiation shielding with cobalt-titania hybrid nanomaterials, *Sci. Rep.*, 2023, **13**(1), 8936.

30 O. Aviles-Garcia, J. Espino-Valencia, R. Romero-Romero, J. Rico-Cerda, M. Arroyo-Albiter, D. Solis-Casados and R. Natividad- Rangel, Enhanced photocatalytic activity of titania by co-doping with Mo and W, *Catalyst*, 2018, **8**, 631.

31 A. F. Tag El-Din, E. A. Elshehy and M. E. El-Khouly, Cellulose acetate/EDTA-chelator assisted synthesis of ordered mesoporous HAp microspheres for efficient removal of radioactive species from seawater, *J. Environ. Chem. Eng.*, 2018, **6**, 5845.

32 E. A. Elshehy, Removal of uranium ions from liquid radioactive waste using modified aluminosilica, *Sep. Sci. Technol.*, 2017, **52**, 1852.

33 M.-C. Wu, J.-S. Chih and W.-K. Huang, Bismuth doping effect on TiO_2 nanofibres for morphological change and photocatalytic performance, *CrystEngComm*, 2014, **16**, 10692.

34 R. Kaushik, S. Gandhi and A. Halder, Photoelectrochemical Degradation of Organic Pollutants Coupled with Molecular Hydrogen Generation Using Bi_2O_3/TiO_2 Nanoparticle Arrays, *ACS Appl. Nano Mater.*, 2023, **6**, 4297.

35 H. Yadav, S. Otari, R. Bohara, S. Mali, S. Pawar and S. Delekar, Synthesis and visible light photocatalytic antibacterial activity of nickel-doped TiO_2 nanoparticles against Gram-positive and Gram-negative bacteria, *J. Photochem. Photobiol.*, 2014, **A294**, 130.

36 L.-L. Lai, W. Wen and J.-M. Wu, Ni-doped rutile TiO_2 nanoflowers: low-temperature solution synthesis and enhanced photocatalytic efficiency, *RSC Adv.*, 2016, **6**, 25511.

37 J.-Q. Bai, W. Wen and J.-M. Wu, Facile synthesis of Ni-doped TiO_2 ultrathin nanobelt arrays with enhanced photocatalytic performance, *CrystEngComm*, 2016, **18**, 1847.

38 M. P. Blanco-Vega, J. L. Guzmán-Mar, M. Villanueva-Rodríguez, L. Maya-Treviño, L. L. Garza-Tovar, A. Hernández-Ramírez and L. Hinojosa-Reyes, *Mater. Sci. Semicond. Process.*, 2017, **71**, 275.

39 S. Sajjad, S. A. Leghari, F. Chen and J. Zhang, Bismuth-Doped Ordered Mesoporous TiO_2: Visible-Light Catalyst for Simultaneous Degradation of Phenol and Chromium, *Chemistry*, 2010, **16**, 13795.

40 H. Li, D. Wang, P. Wang, H. Fan and T. Xie, Synthesis and Studies of the Visible-Light Photocatalytic Properties of Near-Monodisperse Bi-Doped TiO_2 Nanospheres, *Chemistry*, 2009, **15**, 12521.

41 H. Fan, G. Wang and L. Hu, Infrared, Raman and XPS spectroscopic studies of Bi_2O_3-B_2O_3-Ga_2O_3 glasses, *Solid State Sci.*, 2009, **11**, 2065.

42 P. A. K. Reddy, B. Srinivas, P. Kala, V. D. Kumari and M. Subrahmanyam, Preparation and characterization of Bi-doped TiO_2 and its solar photocatalytic activity for the degradation of isoproturon herbicide, *Mater. Res. Bull.*, 2011, **46**, 1766.

43 S. Estrada-Flores, C. M. Pérez-Berumen, T. E. Flores-Guia, L. A. García-Cerda, J. Rodríguez-Hernández, T. A. Esquivel-Castro and A. Martínez-Luévanos, Mechanosynthesis of Mesoporous Bi-Doped TiO_2: The Effect of Bismuth Doping and Ball Milling on the Crystal Structure, Optical Properties, and Photocatalytic Activity, *Crystals*, 2022, **12**, 1750.

44 V. Katheresan, J. Kansedo and S. Lau, Efficiency of various recent wastewater dye removal methods: A review, *J. Environ. Chem. Eng.*, 2018, **6**, 4676.

45 H. Zhu, R. Jiang, Y. Fu, Y. Guan, J. Yao, L. Xiao and G. Zeng, Effective photocatalytic decolorization of methyl orange utilizing TiO_2/ZnO/chitosan nanocomposite films under simulated solar irradiation, *Desalination*, 2012, **286**, 41.

46 S. Abbasi, M. Hasanpour, F. Ahmadpoor, M. Sillanpää, D. Dastan and A. Achour, Application of the statistical analysis methodology for photodegradation of methyl orange using a new nanocomposite containing modified TiO_2 semiconductor with SnO_2, *Int. J. Environ. Anal. Chem.*, 2019, **101**, 208.

47 H. Lachheb, E. Puzenat, A. Houas, M. Ksibi, E. Elaloui, C. Guillard and J.-M. Herrmann, Photocatalytic degradation of various types of dyes (Alizarin S, Crocein Orange G, Methyl Red, Congo Red, Methylene Blue) in water by UV-irradiated titania, *Appl. Catal., B*, 2002, **39**, 7590.

48 Y. Ding, C. Yang, L. Zhu and J. Zhang, Photoelectrochemical activity of liquid phase deposited TiO_2 film for degradation of benzotriazole, *J. Hazard. Mater.*, 2010, **175**, 96–103.

49 M. S. Khan, C. F. Kait and M. I. Abdul Mutalib, Photooxidative desulfurization for diesel using Fe/N-TiO_2 photocatalyst, *AIP Conf. Proc.*, 2014, **1621**, 10.

50 M. Khan, J. Shah, M. Arshad, S. A. Halim, A. Khan, A. J. Shaikh, N. Riaz, A. J. Khan, M. Arfan, M. Shahid, A. Pervez, A. A. Harasi and M. Bilal, Photocatalytic Decolorization and Biocidal Applications of Nonmetal Doped TiO_2: Isotherm, Kinetic, Modeling and In Silico Molecular Docking Studies, *Molecules*, 2020, **25**, 4468.

51 S. Sowmya, G. Madhu and M. Hashir, Studies on Nano-Engineered TiO_2 Photo Catalyst for Effective Degradation of Dye, *IOP Conf. Ser.: Mater. Sci. Eng.*, 2018, **310**, 012026.

52 M. Moradi, F. Khorasheh and A. Larimi, Pt nanoparticles decorated Bi-doped TiO_2 as an efficient photocatalyst for CO_2 photo-reduction into CH_4, *Sol. Energy*, 2020, **211**, 100–110.

53 L. Deng, B. Chang, D. Shi, X. Yao, Y. Shao, J. Shen, B. Zhang, Y. Wu and X. Hao, MXene decorated by phosphorus-doped TiO_2 for photo-enhanced electrocatalytic hydrogen evolution reaction, *Renewable Energy*, 2021, **170**, 858–865.

54 J. Yu, B. Chang, W. Yu, X. Li, D. Wang, Z. Xu, X. Zhang, H. Liu and W. Zhou, Chromium phosphide nanoparticles embedded in porous nitrogen-/phosphorus-doped carbon as efficient electrocatalysts for a nitrogen reduction reaction, *Carbon Energy*, 2022, **4**(2), 237–245.

55 F. Hasanvandian, M. Zehtab Salmasi, M. Moradi, S. Farshineh Saei, B. Kakavandi and S. Rahman Setayesh, Enhanced spatially coupling heterojunction assembled from $CuCo_2S_4$ yolk-shell hollow sphere capsulated by Bi-modified TiO_2 for highly efficient CO_2 photoreduction, *Chem. Eng. J.*, 2022, **444**, 136493.